The X-ray emission from shock cooling zones in O star winds[*]

A. Feldmeier[1], R.-P. Kudritzki[1,2], R. Palsa[1], A.W.A. Pauldrach[1], and J. Puls[1]

[1] Institut für Astronomie und Astrophysik der Universität, Scheinerstr. 1, D-81679 München, Germany
[2] Max-Planck-Institut für Astrophysik, Karl-Schwarzschild-Str. 1, D-85740 Garching, Germany

Abstract. A semi-empirical model is developed for the X-ray emission from O star winds, and used to analyze recent ROSAT PSPC spectra. The X-rays are assumed to originate from cooling zones behind shock fronts, where the cooling is primarily radiative at small radii in the wind, and due to expansion at large radii. The shocks are dispersed in a cold background wind whose X-ray opacity is provided by detailed NLTE calculations.

This model is a natural extension of the Hillier et al. (1993) model of isothermal wind shocks. By assuming spatially constant shock temperatures, these authors achieved good fits to the data only by postulating two intermixed shock families of independent temperature and filling factor – i.e., by adjusting in parallel four parameters. By applying the present model to the analysis of high S/N PSPC spectra of three O-stars (ζ Pup, ι Ori, ζ Ori), we achieve fits of almost the same quality with only two parameters. This supports the idea that the two- or multi-component X-ray spectra are indeed due to stratified cooling layers.

Key words: hydrodynamics – radiative transfer – shock waves – stars: early-type – X-rays: stars

1. Introduction

The X-ray satellite ROSAT, with its high energy resolution and sensitivity, in particular at soft photon energies, is an ideal tool to investigate the nature of the X-ray emission of hot, luminous stars. Hillier et al. (1993) presented a high quality ROSAT PSPC spectrum of the O4 I(f) star ζ Pup over the energy range from 0.1 to 2.5 keV. They were able to interpret this spectrum by a simple model in which the X-rays arise from shocks distributed with a constant filling factor throughout the wind. A large fraction of the emission from these shocks is absorbed by the ambient cool wind material, for which the wavelength dependent opacity is calculated from detailed non-LTE stellar wind models. As it turns out, this cool wind opacity is crucial for the emergent

X-ray spectrum which shows a maximum at 0.85 keV and a significant drop towards lower energies (cf. Fig. 10).

Hillier et al. achieved a reasonable fit to the observations with the assumption that all shocks were characterized by a single temperature of $\log T$ [K] ≈ 6.60 (see their Fig. 2). But the flux deficiency in the calculated spectrum for energies below 0.45 keV indicated that a cooler shock component of $\log T \approx 6.30$ and of roughly equal filling factor as the hotter component should be present (Fig. 4 of Hillier et al., and Fig. 10 of the present paper). For the B bright giant ϵ CMa (B2 II), on the other hand, Drew et al. (1994) and Cohen et al. (1996) claim that a one-temperature model is incapable of explaining the ROSAT spectrum, while good fits can be achieved with a two-temperature model.

Generally, the wind shocks should have a cooling zone of decreasing temperature and increasing density that contributes significantly to the X-ray spectrum (cf. Krolik & Raymond 1985). Therefore, the use of a one- or two-temperature hot plasma emission coefficient, while valuable for the ad hoc characterization of shock properties for individual hot stars, is of course questionable. Consequently, it is important to investigate how the structure of a cooling zone behind the shock modifies the emission coefficient and the theoretical emergent X-ray spectrum.

Such an investigation is the purpose of the present paper. We extend the concept of randomly distributed shocks embedded in the absorbing cool wind, as used by Hillier et al., and replace their mono-temperature integral over the emitting region to account for cooling gas behind the shock front. We adopt simple approximations (§2) for the shock structure in the inner region of a stellar wind, where the cooling time is shorter than the flow time and the shocks are radiative; and for the outer regions, where the shocks are non-radiative, i.e., they only cool by adiabatic expansion. In §3, we apply this model to three O stars with high signal-to-noise ROSAT PSPC spectra to test how the theoretical X-ray spectrum is modified by the introduction of structured shocks. A summary of the results is given in §4.

2. Simple post-shock models

Since radiation driven winds are inherently unstable (Lucy & Solomon 1970; Carlberg 1980; Owocki & Rybicki 1984, 1985;

Lucy 1984), it is reasonable to attribute the X-ray emission of hot stars to shocks in their stellar winds. Hillier et al. (1993) considered non-stratified, isothermal shocks, where the density and temperature of the hot gas behind the front are constant with radius. The energy emitted by hot gas from a volume dV into the full solid angle 4π is

$$\epsilon_\nu(r) = e_s(r)\, n_p(r)\, n_e(r)\, \Lambda_\nu(n_e(r), T_s(r))\, dV \quad [\text{erg/s}]. \tag{1}$$

Here, $n_p(r)$ is the proton density, $n_e(r)$ the electron density, $T_s(r)$ the temperature, and $e_s(r)$ the volume filling factor of hot gas behind a shock front located at radius r. The frequency dependent cooling function of a hot plasma, Λ_ν, is calculated using the most recent version of the Raymond-Smith code (Raymond & Smith 1977). Hillier et al. neglected the density dependence in the argument of Λ_ν and adopted $\Lambda_\nu = \Lambda_\nu(10^{10}\ \text{cm}^{-3}, T_s)$ throughout the wind, which is a good approximation that we also used in the following. To avoid any further explicit reference to the density of the hot post-shock gas, we redefine the filling factor so that n_p and n_e in (1) (and in subsequent equations) are the *stationary*, 'cool' wind densities. Notice that we do not introduce a factor of 16 here as did Hillier et al. (1993) to account for the density jump at a strong shock. The present definition is more convenient to compare the filling factors from different models of the X-ray emission from hot star winds with differing densities of hot gas.

To account for the temperature and density stratification in the shock cooling layer, ϵ_ν is replaced by an integral over this zone,

$$\hat{\epsilon}_\nu(r) = e_s(r)\, n_p(r)\, n_e(r)\, \hat{\Lambda}_\nu(T_s(r))\, dV,$$

$$\hat{\Lambda}_\nu(T_s(r)) = \pm \frac{1}{L_c} \int_{r}^{r \pm L_c} f^2(r')\, \Lambda_\nu(T_s(r)\, g(r'))\, dr', \tag{2}$$

where r is again the location of the shock front, and r' is the coordinate in the cooling layer of extent L_c. The '+' sign corresponds to a reverse shock, the '−' sign to a forward shock. The functions f and g describe the normalized density and temperature stratification in the post-shock region, respectively. $f = g = 1$ returns the non-stratified, isothermal shocks. With the introduction of the dimensionless coordinate

$$\xi = 1 - \frac{|r - r'|}{L_c}, \tag{3}$$

$\hat{\Lambda}_\nu$ can be written as (using the same symbols f and g again)

$$\hat{\Lambda}_\nu(T_s) = \int_0^1 f^2(\xi)\, \Lambda_\nu(T_s\, g(\xi))\, d\xi. \tag{4}$$

In principle, the functions $f(\xi)$ and $g(\xi)$ have to be calculated from time-dependent hydrodynamic simulations of radiation driven winds. This is the topic of a forthcoming paper. In the present paper we take a first step by using simplified analytical models for the radiative and adiabatic shocks typically found in such numerical calculations.

2.1. Stationary radiative shocks

The decisive quantity to distinguish between alternative post-shock models is the cooling time, t_c, required by the shocked matter to return to the ambient wind temperature again,

$$t_c = \frac{L_c}{v_{po}} \int_0^1 \frac{d\xi}{h(\xi)}. \tag{5}$$

Here, $h = |v - v_s|/v_{po}$, where v and v_s are the wind speed and the shock speed, respectively, in the stellar frame; v_{po} is the absolute value of the speed of post-shock gas (i.e., gas immediately behind the front) relative to the front. Therefore, $v_{po}h(\xi)$ is the speed of gas in the cooling zone relative to the shock front. If t_c is small compared with the dynamical flow time t_f,

$$t_f = \frac{r}{v(r)}, \tag{6}$$

the shock can be regarded as stationary.

Because of the very high temperature in the post-shock region, the radiative acceleration of matter can be neglected. The same is true for gravitational acceleration, since for strong shocks the gravity scale height is large compared with the cooling length L_c. In such a case then, the post-shock structure is given by the stationary, 1-D plane-parallel gasdynamic equations, which include radiative cooling in the energy equation. This problem has been discussed by Chevalier & Imamura (1982; CI in the following) for special cases, where the frequency integrated cooling function follows a power law in temperature,

$$\Lambda(T) = \int_0^\infty \Lambda_\nu(T)\, d\nu = A_R\, T^\alpha. \tag{7}$$

In the following we shall use $A_R = 1.64 \times 10^{-19}\ \text{erg cm}^3\ \text{s}^{-1}\ \text{K}^{1/2}$ and $\alpha = -1/2$ as a reasonable approximation to the cooling function of a hot plasma for temperatures in the range $10^{4.8} \leq T \leq 10^{7.3}$ K (Cox & Tucker 1969; Raymond et al. 1976). Extending the analysis of CI to the cooling exponent $\alpha = -1/2$, we obtain the solution

$$f(\xi) = \frac{1}{h(\xi)},$$

$$g(\xi) = \tfrac{1}{3}\, h(\xi)(4 - h(\xi)),$$

$$\xi(h) = \frac{1}{93\sqrt{3} - 40\pi} \left\{ -120 \arccos\left(1 - \tfrac{1}{2}h\right) \right.$$
$$\left. + \sqrt{4h - h^2}\, \left(60 + 10h + 2h^2 + 29h^3 - 8h^4\right)\right\}, \tag{8}$$

where $0 \leq h \leq 1$. The total cooling time and cooling length are

$$t_c = \frac{40}{7} \frac{C}{A_R} \frac{v_{po}^3}{\rho_{po}},$$

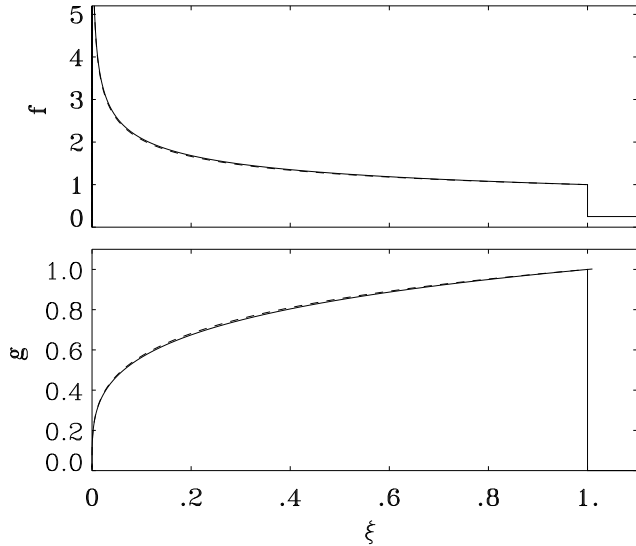$$L_c = \frac{93\sqrt{3} - 40\pi}{10} \frac{C}{A_R} \frac{v_{po}^4}{\rho_{po}}, \tag{9}$$

Fig. 1. Post-shock structure for a steady radiative shock after Eq. (8). The density function f and temperature function g defined in (2) are shown. Dashed line: approximation for f and g after (11).

Fig. 2. Cooling function versus energy for $\log T = 6.6$. Solid: stratified radiative shock emission $\hat{\Lambda}_\nu(T)$; dashed: Raymond-Smith function $\Lambda_\nu(T)$.

where for a hydrogen/helium gas the constant C is given by (with m_p the proton mass, k the Boltzmann constant)

$$C = \frac{m_p^{5/2}}{k^{1/2}} \frac{(1+4Y)^{5/2}}{(1+IY)(2+[1+I]Y)^{1/2}}. \tag{10}$$

The helium fraction by number is $Y = n_{He}/n_H$, and I is the number of free electrons provided per helium nucleus; hydrogen is assumed to be fully ionized. Fig. 1 shows the density function f and the temperature function g.

To the best of our knowledge, the function $\xi(h)$ in (8) cannot be inverted analytically to give $h(\xi)$. From a Taylor expansion at $h = 0$ and the requirement that $h(1) = 1$ at the beginning of the cooling zone, we find

$$h(\xi) = a\,\xi^{2/7}\left[1 + \left(\frac{1}{a} - 1\right)\xi^{2/7}\right], \tag{11}$$

where $a = \left[\frac{7}{10}\left(\frac{93\sqrt{3}}{40} - \pi\right)\right]^{2/7} \approx 0.87225$. This is accurate to better than 1.4% over the *whole* cooling zone, see Fig. 1, and is therefore used in the following.

With (8) and (11), the post-shock structure is well defined and the cooling function of the stratified shock can be calculated according to (4). The result is shown in Fig. 2 for $\log T_s = 6.6$ (for gas of solar composition). The stratified shock emits significantly more radiation at soft energies, and less above 1.3 keV than an isothermal shock. This can be understood from Fig. 3. In the temperature-energy plane the Raymond-Smith function $\Lambda_\nu(T_s)$ has a maximum at ($\log T = 6.25$; $E = 0.5$ keV). According to (4), all layers with $T \leq T_s$ contribute with increasing weight factor f^2 to the cooling function $\hat{\Lambda}_\nu(T_s)$ for structured shocks. For $\log T_s = 6.6$ and $E \leq 0.5$ keV, $\Lambda_\nu(T_s\,g)$ passes the maximum and, thus, $\hat{\Lambda}_\nu(T_s)$ becomes larger than $\Lambda_\nu(T_s)$. For $\log T_s = 6.6$ and $E > 1$ keV, $\Lambda_\nu(T_s)$ decreases
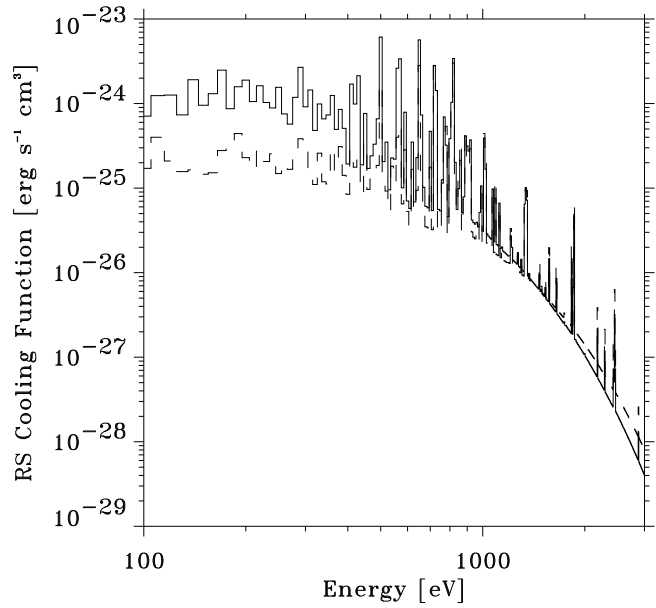
so rapidly that the weighting factor f^2 is not able to compensate and $\hat{\Lambda}_\nu(T_s) < \Lambda_\nu(T_s)$ results. Fig. 4 shows the ratio $\hat{\Lambda}_\nu/\Lambda_\nu$ in the temperature-energy plane.

To calculate the X-ray emission from an *ensemble* of embedded wind shocks, we need to know the shock temperature T_s and the filling factor e_s as functions of radius. Notice that while the density and temperature stratification, f and g, within the cooling zone are 'microscopic' functions, i.e., they depend on short-scale radiative cooling only, T_s and e_s are 'macroscopic' quantities which depend on the actual wind dynamics. One might try however to derive some ad hoc conclusions about them. Concerning the filling factor, a simple argument may proceed as follows: assume for the moment that the shock temperature is independent of radius in regions where the wind has reached a substantial fraction of its terminal velocity. From (9), the cooling length then grows as $L_c \propto 1/\rho \propto r^2$. If we assume furthermore that no shocks are created beyond a certain location in the wind, and that the shocks are also not destroyed on their further propagation, the filling factor grows as $e_s \propto r^2$.

However, time-dependent hydrodynamic simulations (Owocki et al. 1988; Owocki 1992; Feldmeier 1995) of initially small perturbations which grow in an unstable wind confirm these conclusions only partially[1]: here, the shock temperatures and shock spacing result from complex wind dynamics, which

---

[1]   In these simulations, the smooth, stationary wind is usually transformed into a sequence of narrow, dense shells, which are separated by almost void regions. On their starward side, the shells are bound by a strong reverse shock, which decelerates a fast, inner wind stream. On their outer side, they are bound by a weak forward shock which overtakes the slower gas ahead of it (at larger radii), and compresses it into the shell.
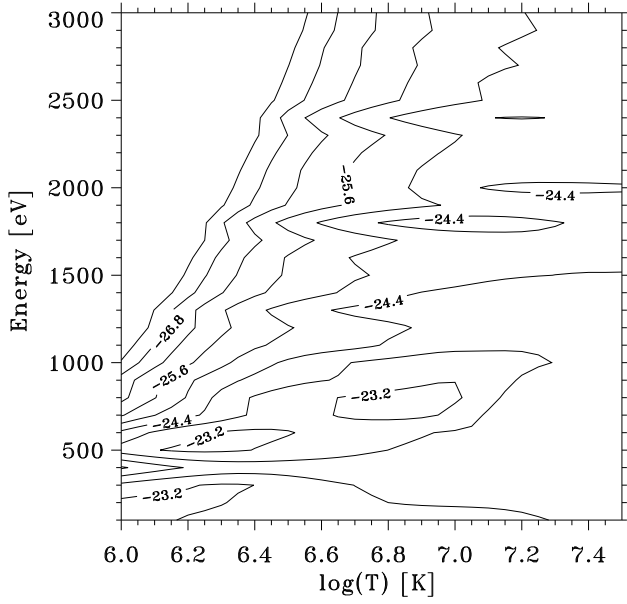
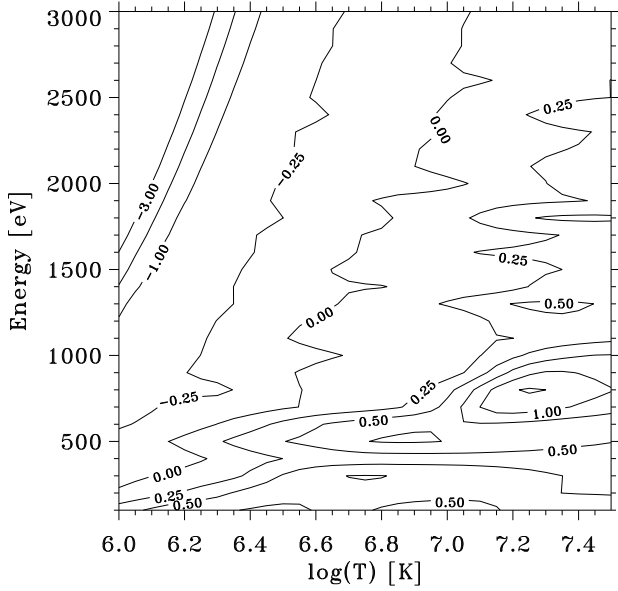**Fig. 3.** Isocontours of log Λ_ν in the log T–energy plane.

Fig. 4. Isocontours of log $(\hat{\Lambda}_\nu/\Lambda_\nu)$ in the log T–energy plane.

from variability observations of hot stars (cf. the volume edited by Moffat et al. 1994). Thus, for simplicity, we shall suppose in the following constant T_s and e_s throughout the wind.

Two further important restrictions have to be made. The first one concerns the thermal instability of radiative shocks. Langer et al. (1981, 1982) and CI have pointed out that for temperature exponents $\alpha \lesssim 1$ in the cooling function power law (7), a global thermal instability exists that leads to a periodic contraction and expansion of the cooling zone, i.e., to an oscillation in the position of the shock. The typical timescale of this oscillation is of the order of a few cooling times. Since the density and temperature stratification of the post-shock region change during the course of this contraction and expansion, and since these quantities enter non-linearly into the shock emission coefficient, the thermal instability will certainly affect the emitted spectrum. In the model presented here, we have simply neglected these effects to keep them analytically tractable.

The second restriction is given by the assumption that the cooling time t_c is small compared with the dynamical flow time t_f. We expect that far out in the wind at low densities, t_c will become larger than t_f and the assumption will fail. Using the stationary wind velocity law (where $\hat{r} \equiv r/R_*$, v_∞ is the terminal velocity, and with assumed value of $\beta = 1$),

$$v(r) = v_\infty \left(1 - \frac{b}{\hat{r}}\right), \qquad b = 0.99, \tag{12}$$

and the equation of continuity together with (6) and (9), we obtain for the ratio of cooling to flow time (where $\dot{M}$ is the mass loss rate; and T_6 is the temperature in units of 10^6 K),

$$\frac{t_c}{t_f} = 5.37 \times 10^{-4} \left(\frac{v_\infty}{10^3 \text{ km/s}}\right)^2 \left(\frac{\dot{M}}{10^{-6} \text{ M}_\odot/\text{yr}}\right)^{-1} \frac{R_*}{10\, R_\odot} \times$$
$$\frac{(1+4Y)(2+[1+I]Y)}{1+IY} T_{s,6}^{3/2}\, \hat{r}\left(1 - \frac{b}{\hat{r}}\right)^2, \tag{13}$$

and for the ratio of the cooling length to the position of a shock, r_s,

$$\frac{L_c}{r_s} = 1.75 \times 10^{-5} \frac{v_\infty}{10^3 \text{ km/s}} \left(\frac{\dot{M}}{10^{-6} \text{ M}_\odot/\text{yr}}\right)^{-1} \frac{R_*}{10\, R_\odot} \times$$
$$\frac{(1+4Y)^{1/2}(2+[1+I]Y)^{3/2}}{1+IY} T_{s,6}^2\, (\hat{r} - b). \tag{14}$$

For the O star ζ Pup, e.g., we find from Table 1 (using $I = 1$, cf. Sect. 3),

$$\frac{t_c}{t_f} = 2.59 \times 10^{-3}\, T_{s,6}^{3/2}\, \hat{r}\left(1 - \frac{b}{\hat{r}}\right)^2,$$
$$\frac{L_c}{r_s} = 4.62 \times 10^{-5}\, T_{s,6}^2\, (\hat{r} - b). \tag{15}$$

For $T_s = 5 \times 10^6$ K, e.g., we obtain for ζ Pup $r_0 = 36\, R_*$ for the radius at which t_c/t_f is unity. At this radius, $L_c/r_s = 0.04$ is still small.

lead to frequent mergers of shocks. Notice that the latter falsify the above assertion that shocks should keep their identity. The results from these calculations are broadly consistent with constant or slowly decreasing temperatures *and* filling factors of hot gas as a function of radius. However, the details of the wind dynamics are still largely unknown, (i) due to approximations in the treatment of the radiative transfer, the small-scale structure in the wind, and thermal instabilities (see below); and (ii) since neither the location (photosphere vs. wind), the nature (pulsations, waves, noise, etc.), nor the temporal coherence (periodic vs. stochastic) of the seeding perturbations are known at present

However, as discussed before, the actual wind dynamics may be far from stationary, and due to the progressive accumulation of the wind gas into dense shells, these values for r_0 may be (much) too large. This is discussed further in the next section.

For X-ray photons which stem from radii larger than r_0, the approximations made in this section will be invalid. Consequently, we next study an alternative approximation that will hold for locations beyond r_0.

2.2. Constant velocity adiabatic shocks

Far out in the wind, where $r \gg r_0$, the radiative cooling of the shocks can be neglected. We thus expect spherical segments of shocks that started at much smaller radii will expand undergoing adiabatic cooling only. In addition, the unperturbed wind has achieved its terminal velocity and radiative acceleration is small. Simon & Axford (1966; SA in the following) have treated such a problem for a pair of reverse-forward shock waves which propagate at constant velocity through the outer solar wind and/or interplanetary medium. As mentioned before, such pairs of shocks which enclose a shell of dense material are also expected from time-dependent hydrodynamic simulations of hot star winds.

SA solve the spherical problem of a driven shell (see below for the precise meaning) in terms of the similarity variable

$$\eta = \frac{r}{v_f t}, \tag{16}$$

where v_f is the velocity of the forward shock front, which is therefore located at $\eta_f = 1$. (At $t = 0$, the whole shell is at $r = 0$.)

This similarity variable is appropriate only for the case that all flow features (shocks and contact discontinuities) move at constant speeds. As discussed by SA, this corresponds to a temporally constant mass loss rate of the source after the shell release, where the latter is caused by a sudden jump of the density and velocity (and therefore, usually, of the mass loss rate; cf. Appendix A). The general case of a similarity variable $\eta = r/At^\delta$ corresponds to a time dependence $v_f \propto t^{\delta-1}$ of the speed of all flow features, and a change in mass loss rate $\dot{M} \propto t^{\delta-1}$ of the source after throwing off the shell. This temporal behaviour of source conditions is meant to mimic a solar flare and the subsequent return to the quiescent wind. – However, for the *radiation* driven winds of hot stars it is at present not clear how the non-similarity dynamics at small radii serves as an inner boundary condition for the similarity solution (possibly) achieved at large distances. As discussed in the foregoing section, this is both due to the unknown nature of the wind perturbations, and to the intricate shock dynamics with frequent merging, etc. (in Appendix B we shall demonstrate for a simple example how shock collisions can influence the propagation characteristics of the shocks, i.e., the parameter δ). In particular, it seems possible that the outer, adiabatic flow belongs to the class of similarity problems for which, according to Zel'dovich & Raizer (1967,

Chap. XII, p. 794), the "self-similar motion originates as a result of some non-selfsimilar flow that approaches a self-similar regime asymptotically", and where the similarity exponent δ cannot be determined in advance by dimensional considerations or from the conservation laws, but has to be found from the actual solution of the problem. In light of these uncertainties, our assumption of constant shock speeds and therefore constant shock temperatures in the outer similarity regime appears to be a reasonable 'minimum hypothesis'.

One may then try to derive the radial dependence of the filling factor e_s of the completely macroscopic (T_s, e_s and f, g) adiabatic shocks: since all shells move at the same speed, and since the forward shocks propagate faster than the reverse shocks, every forward shock should eventually overtake the reverse shock of the neighboring shell ahead of it. As long as all shock speeds remain constant, and the distance between successive shells is small compared with the radii the shells are located at, $e_s \propto r$. However, as shown in Appendix B, this does not imply the existence of an outer, hot corona. Instead, the filling factor of hot gas always remains < 1 (or even $\ll 1$), while it is the fraction of gas which passed through a shock transition which approaches unity.

Furthermore, time-dependent wind simulations of unstable growth show that many (if not most) radiative reverse shocks, instead of being progressively transformed into adiabatic reverse shocks at large radii $r_0 \gg 10\, R_*$, are suddenly destroyed at intermediate radii $\lesssim 10\, R_*$, and leave behind hot, adiabatic cooling gas which was heated in the front at previous times (Feldmeier 1995). – Due to these two processes of shock merging and shock destruction, a monotonically decreasing or roughly constant filling factor is more appropriate than the increasing filling factor asserted above. In the following, a constant e_s will be supposed.

Finally, in the comparison with observations it is important to realize that exposure times of ROSAT are of the order of some 1000 seconds, whereas for $r \gtrsim 100\, R_*$ the flow time is some 10^5 seconds. Therefore, every exposure reflects the momentary position and stratification of shocks in the outer wind. As a consequence, the post-shock solutions $\rho(\eta)$ and $T(\eta)$ obtained by SA describe purely spatial structures in our case, since the time t in the definition of η can be regarded as constant for every exposure.

In terms of the similarity variable from (16), the hydrodynamic quantities are written as

$$v(r,t) = \frac{rV(\eta)}{t}, \quad \rho(r,t) = \frac{\rho_0 \sigma(\eta)}{r^2}, \quad p(r,t) = \frac{\rho_0 \pi(\eta)}{t^2}. \tag{17}$$

Note that the velocity of *every* flow feature f, i.e., shocks and contact discontinuities, is then $V_f \equiv 1$, since $v_f = r_f V_f/t$ and also $v_f = r_f/t$.

The positions of the reverse shock, η_r, and the contact discontinuity inside the shell, η_c, are found from numerical integration of the ordinary differential equation (10) of SA. The two integration constants which determine a special solution are chosen to be
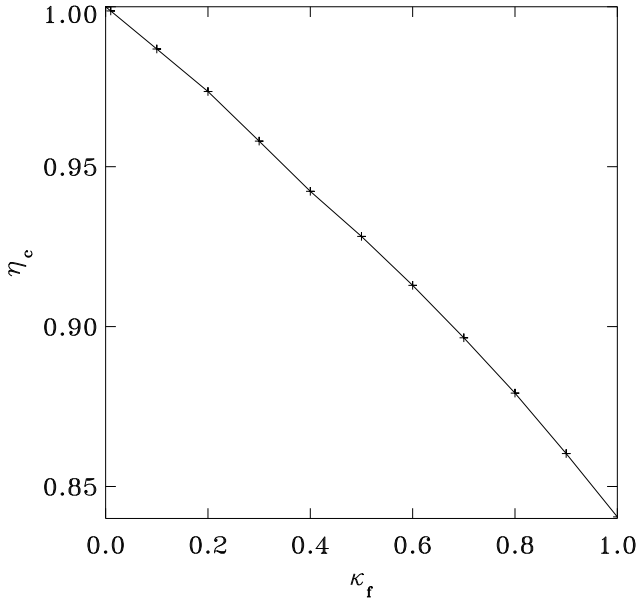
Fig. 5. Dependence of the position η_c of the contact discontinuity on the inflow parameter $\kappa_f = v_{f,pr}/v_f$.

$$\kappa_f = v_{f,pr}/v_f,$$
$$\Theta = T_{r,po}/T_{f,po}. \tag{18}$$

Here and in the following, indices 'r' and 'f' refer to the reverse and forward shock, respectively. SA fixed $\kappa_f = 1$ for the solar wind by neglecting the ambient wind speed as compared with the forward shock speed. In general, for a non-negligible speed v_∞ ahead of the forward shock, one finds (with μ the mean atomic weight)

$$\kappa_f = \left(1 + \frac{3}{4}\frac{v_\infty}{v_{f,ju}}\right)^{-1} = \left(1 + \sqrt{\frac{3\mu m_p}{16k}}\frac{v_\infty}{\sqrt{T_{f,po}}}\right)^{-1}, \tag{19}$$

where v_{ju} is the velocity jump across the shock, and in the first equality $v_{pr} = \frac{4}{3}v_{ju}$ and $v_f = v_{hi} + \frac{1}{3}v_{ju}$ (with v_{hi} the velocity immediately behind the shock front) have been used for a strong shock in a gas with $\gamma = 5/3$. For typical O star wind speeds, and temperatures of the forward shock up to 10^7 K, $0 \leq \kappa_f \leq 0.3$.

The position of the contact discontinuity and of the reverse shock are then functions of κ_f and Θ,

$$\eta_c = \eta_c(\kappa_f),$$
$$\eta_r = \eta_r(\kappa_f, \Theta). \tag{20}$$

The (numerically derived) function $\eta_c(\kappa_f)$ is shown in Fig. 5. A good fit to this is

$$\eta_c = 1 - 0.1314\kappa_f - 0.02857\kappa_f^2. \tag{21}$$

The function $\eta_r(\kappa_f, \Theta)$ is determined by Fig. 6. For different values of κ_f, Fig. 6 shows the dependence of the ratio of the

cooling lengths of the reverse and forward shock, $(\eta_c - \eta_r)/(1 - \eta_c)$, on Θ. In the range $0 \leq \kappa_f \leq 0.3$, this can be approximated by

$$\frac{\eta_c - \eta_r}{1 - \eta_c} = (1 - \kappa_f + \kappa_f^2)\,\Theta^{\frac{1}{2} - 0.31\kappa_f + 0.55\kappa_f^2}. \tag{22}$$

From Fig. 6 (and also from the foregoing equation),

$$\lim_{\kappa_f \to 0} \frac{\eta_c - \eta_r}{1 - \eta_c} = \sqrt{\Theta}, \tag{23}$$

or, stated differently: for every adiabatic shock with small cooling length (i.e., with sufficiently low post-shock temperature) the cooling length scales as the square root of the post-shock temperature,

$$\lim_{L_c/r \to 0} L_c \propto \sqrt{T_{po}}. \tag{24}$$

This can be understood as follows. The adiabatic energy equation for a fluid particle is (with d/dt the Lagrangian derivative) $dT/dt = -(\gamma - 1)\,T\,\mathrm{div}\,v$. Therefore, the cooling length scales as $L_c \approx -T(dT/dt)^{-1}\,v_{po} \propto (\mathrm{div}\,v)^{-1}\,v_{po}$. Assuming pressure constancy in the cooling zone (see below) one finds from the Euler equation that the velocity gradient is $v' \approx 0$. Assuming spherical symmetry, it follows that $L_c \propto \frac{r}{2v}\,v_{po}$. For all shocks with a velocity jump which is small compared with the stationary wind flow speed one can identify $v \approx v_{stat}$. Furthermore, since for such weak shocks the cooling zone is short compared with dynamical length scales, $L_c \ll r$, the radius r in the foregoing expression for L_c is a well-defined, single location. Using finally $v_{po} \propto \sqrt{T_{po}}$, the above assertion $L_c \propto \sqrt{T_{po}}$ follows.

Within the cooling layers behind the forward and reverse shocks, the spatial post-shock coordinate ξ introduced in (3) can be related to η by

$$\eta = \eta_c + \xi(1 - \eta_c) \quad \text{forward shock,}$$
$$\eta = \eta_c - \xi(\eta_c - \eta_r) \quad \text{reverse shock,} \tag{25}$$

where $0 \leq \xi \leq 1$.

SA give a power-law expansion (their Eq. 11) for the density and temperature in the neighborhood of the contact discontinuity, that leads to the following functions f and g in (2) (the first position in the braces corresponds to the forward shock, the second to the reverse shock),

$$f(\eta) = \{1, \Theta^{-1}\}\left(\frac{\eta_{\{f,r\}}}{\eta}\right)^2 h(\eta)^{-4/9},$$

$$g(\eta) = \frac{1}{f(\eta)},$$

$$h(\eta) = \frac{(\eta_c/\eta)^3 - 1}{(\eta_c/\eta_{\{f,r\}})^3 - 1}. \tag{26}$$

Again we defined $f_f = g_f = 1$ immediately behind the forward shock (notice that $\sigma(\eta) \equiv 4\eta^2 f(\eta)$, since SA use the convention $\sigma_{f,pr} = 1$). In taking $g = 1/f$, we assume the pressure to
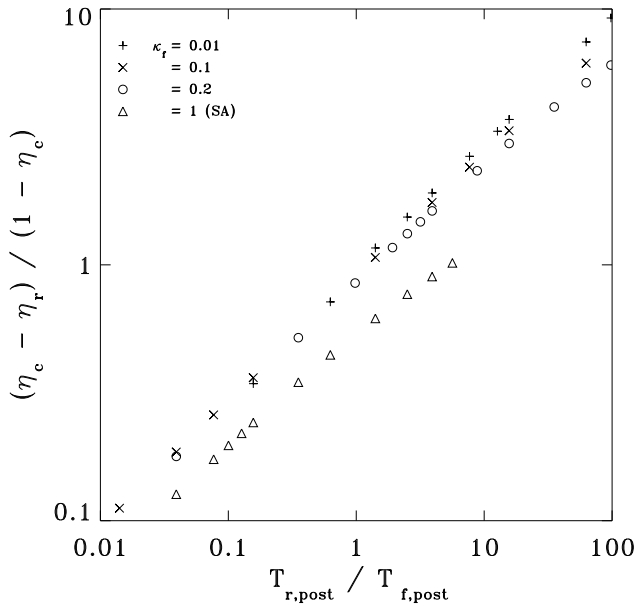
Fig. 6. Dependence of the ratio of the cooling lengths of the reverse and forward shock, $(\eta_c - \eta_r)/(1 - \eta_c)$, on the shock temperature ratio Θ, for different values of the inflow parameter κ_f.
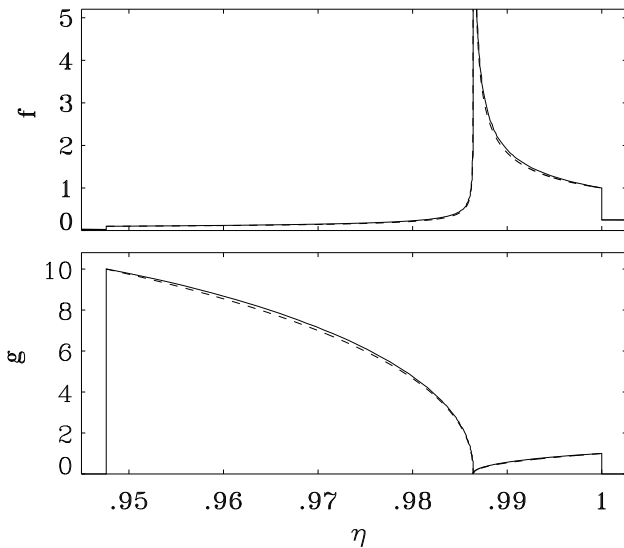

Fig. 7. Full line: exact numerical solution for the SA shell ($\kappa_f = 0.1; \Theta = 10$). Dashed line: approximate analytical solution (26).

be constant through both cooling zones, $\pi_{po} = \frac{3}{4}\kappa_f^2$, which is actually a very good approximation (cf. SA). This pressure constancy also allowed us to fix the density at the reverse shock. As can be seen from Fig. 7, the expansion (26) also describes the overall run, found by numerical integration, of f and g within the cooling zones very well, and is therefore used to calculate the emission coefficient (2) analytically.

Comparing Figs. 1 and 7, one sees that the cooling in the adiabatic shock proceeds more uniformly (i.e., the change in slope over the cooling zone is smaller) than in the radiative
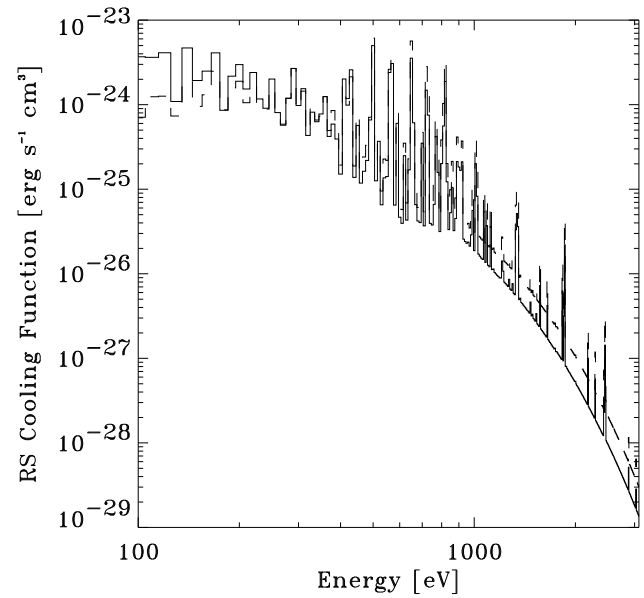

Fig. 8. Cooling function versus energy for $\log T = 6.6$ of an adiabatic shock with $\Theta = 1$ (full line) and of a radiative shock (dashed line).

shock. The reason is that the gas in the radiative shock undergoes runaway cooling (Field 1965), i.e., it cools the better the colder and therefore denser it already is. This is also reflected in Fig. 8 where the cooling functions of an adiabatic shock ($\Theta = 1$ is used here) and a radiative shock of temperature $\log T = 6.6$ are shown. The adiabatic shock has more emission at low energies, and less emission at high energies than the radiative shock; i.e., the adiabatic shock has the softer spectrum.
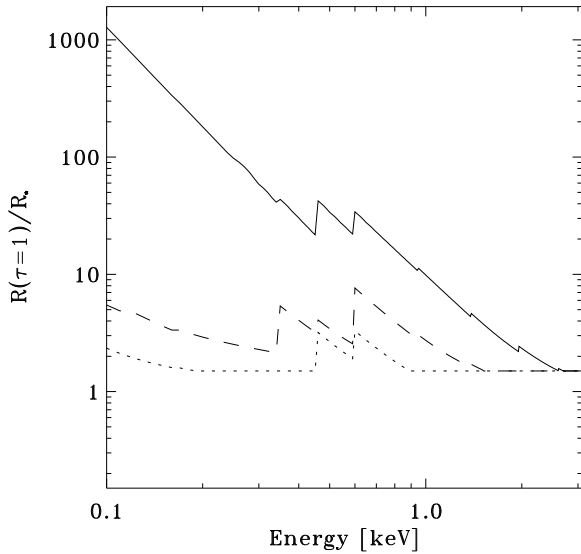
3. Spectral fits for three selected O stars

We assume that the shock temperature, T_s, and the volume filling factor, e_s, have one single, unique value (i) for radiative and adiabatic shocks, and (ii) for reverse and forward shocks. T_s and e_s are then the only two parameters to fit the X-ray spectrum. These restrictions are again meant to make our model directly comparable to the Hillier et al. model, with the one central difference that we use structured cooling zones behind shocks instead of isothermal shocks. We solve the X-ray transfer via a formal integral, where the wind flow is assumed to be spherically symmetric. The X-ray emission is given by (2). (As in Hillier et al., we assume that no X-rays are emitted from below $R_{min} = 1.5\ R_*$.) The bound-free and line opacities for the cold background wind are taken from full NLTE models, and the K-shell opacity is treated for the elements C, N, O, Ne, Mg, Si, S (Daltabuit & Cox 1972).

In the following we present results for the three O stars from Table 1. (The analysis of the full sample of 42 O stars observed with the ROSAT PSPC is topic of a forthcoming publication; preliminary results are given in Kudritzki et al. 1996). They should be ideal candidates to test our X-ray model since they have among the highest signal-to-noise ratio within our full sam-

Table 1. Parameters of the analyzed O stars.

star	classif.	$\frac{T_{\text{eff}}}{10^3 \, \text{K}}$	$\log g$	$\frac{R_*}{R_\odot}$	Y	$\frac{v_\infty}{\text{km/s}}$	$\frac{\dot{M}}{10^{-6} \, M_\odot/\text{yr}}$	$\log\left(\frac{N_{\text{H}}}{\text{cm}^{-2}}\right)$
ζ Pup	O4 I(f)	42	3.6	19	0.12	2250	5.9	20.00
ι Ori	O9 III	34	3.5	18	0.18	2350	0.8	20.30
ζ Ori	O9.7 Ib	32	3.2	24	0.10	1850	2.4	20.48

Fig. 9. Location of optical depth unity for X-rays in the ROSAT energy band for the three stars from Table 1: ζ Pup (full); ι Ori (dotted); ζ Ori (dashed).

ple. Furthermore, their stellar and wind parameters are known to a good accuracy: for ζ Pup, the photospheric parameters are taken from Kudritzki et al. (1983) with the $\log g$ correction for 'unified' effects and centrifugal forces from Puls et al. (1996). For ι Ori, photospheric parameters are from Lamers & Leitherer (1993) and references therein; and for ζ Ori from Voels et al. (1989). The terminal velocities for all three stars are from Haser (1995). The mass loss rates are from Puls et al. (1996), where for ι Ori and ζ Ori the measurements of Lamers & Leitherer have been reanalyzed. Additionally, the mass loss rate of ζ Ori has been recalibrated to the photospheric parameters from Voels et al. and the terminal velocity from Haser, following the procedure described in Puls et al. Metal abundances (which enter through the opacities) are derived for ζ Pup from an analysis of UV spectra (Pauldrach et al. 1994; Haser 1995). For ι Ori we assume CNO processed material, and for ζ Ori we presently assume solar abundances. Finally, the interstellar hydrogen column densities, N_{H}, are from Shull & van Steenberg (1985) using interstellar Ly-α. This is certainly advantageous over deriving N_{H} from the X-ray fits themselves.

We notice that ζ Ori showed an *episodic* change in its X-ray emission during a period of 2 days from Sep 23 to 25 in 1992, when the count rate in the energy band from 0.6 to 2.4 keV

increased by $\approx 30\%$ (Berghöfer & Schmitt 1994). The latter authors proposed a single, strong reverse shock as the cause. This event is not included in our data set which reaches only to Sep 19, 1992. For ζ Pup, on the other hand, Berghöfer et al. (1996) found a *modulation* of period 16.7 hours and amplitude $\lesssim 10\%$ of the count rate in the energy band from 0.9 to 2.0 keV. This was traced back to periodic density variations at the wind base. Since our data set for ζ Pup covers ≈ 16 cycles of this modulation, the data should define a proper average emission. – In total, we conclude that our present *stationary* model for the X-ray emission should be adequate to analyze the ROSAT observations of the above three program stars.

For the comparison of our model fits with the ROSAT observations we have also to consider sources of uncertainties of the data themselves, especially due to the calibration of the PSPC. As advised by the ROSAT User's Handbook (Oct 1994, draft version) we excluded energies above 2.2 keV when fitting the observed spectrum due to insufficient calibration of the effective area and energy response above 2 keV. The Handbook also recommends not using energies below 0.11 keV (detector channel 11) for observations taken after October 11th 1991. Half of the integration time for ζ Ori, and all the integration time for ζ Pup and ι Ori occurred after this date. Therefore we excluded the first data point in the observed spectrum. Finally, uncertainties in the calibration of the PSPC detector response can account for $\approx 20\%$ of the deviations between model and observation at the prominent dip in the observed spectra near 0.4 keV. We therefore also ignored the 2 to 4 data points in the range from 0.38 keV to 0.48 keV in the fitting procedure.

Fig. 9 shows the location of optical depth unity (with optical depth zero at the observer) in the winds of the three stars from Table 1, for X-ray energies in the ROSAT band. From this figure it is clear that soft X-rays can escape the dense wind of ζ Pup only from large radii. Physically, this is due to the fact that helium starts to recombine to He$^+$ from $\approx 6 \, R_*$, which increases the opacity enormously (cf. Hillier et al. 1993). In contrast, helium stays fully ionized in the winds of ι Ori and ζ Ori up to very large radii. Accordingly, the ROSAT spectrum of ζ Pup (cf. Fig. 10) is harder than that of ι Ori (Fig. 11). The spectrum of ζ Ori in Fig. 12 lies intermediate between the former two. This is mostly due to the larger N_{H} in direction of this star than of ι Ori.

Also shown in Figs. 10, 11, and 12 are our best fits to the ROSAT spectra of ζ Pup, ι Ori, and ζ Ori respectively, together with the fits from the Hillier et al. isothermal shock model assuming one or two hot components. Table 2 gives the post-shock
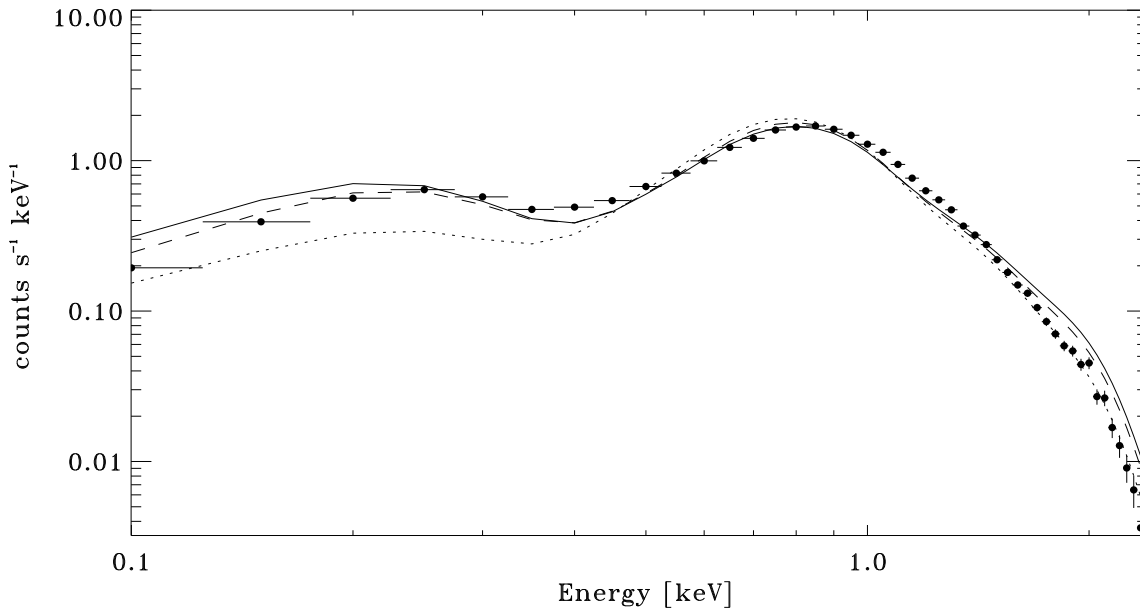
Fig. 10. ROSAT PSPC spectrum of ζ Pup (error bars) together with our best fit (full line) assuming inner radiative and outer adiabatic shocks. For comparison, the best fits from a one-component (dotted line) and two-component (dashed line) isothermal shock model after Hillier et al. (1993) are also shown.
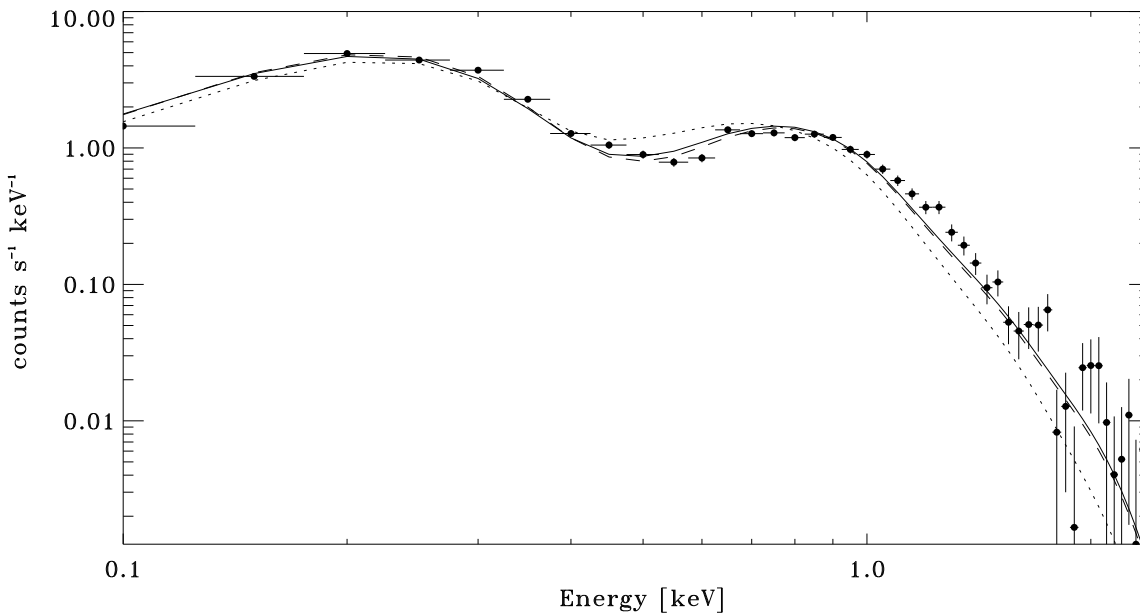

Fig. 11. Spectrum and fits of ι Ori. Labeling of the curves as in Fig. 10.

temperatures and the volume filling factors derived for the three stars. The following conclusions can be drawn from this.

(1) Temperatures: The post-shock temperatures of the present model with resolved cooling zones are, for all three stars, $\approx 30\%$ higher than the temperatures of the hotter shock family of the two-component model after Hillier et al.; they are 60% to 80% higher than the temperatures from their one-component

model. The need for higher temperatures in the present approach is clear from the fact that the Hillier et al. temperatures correspond to averages over the cooling zones.

(2) Filling factors: (a) The sum of the two individual filling factors from the two-component model after Hillier et al. is about equal to the filling factor from their one-component model. (b) The latter is about 2.7 times the filling factor from our
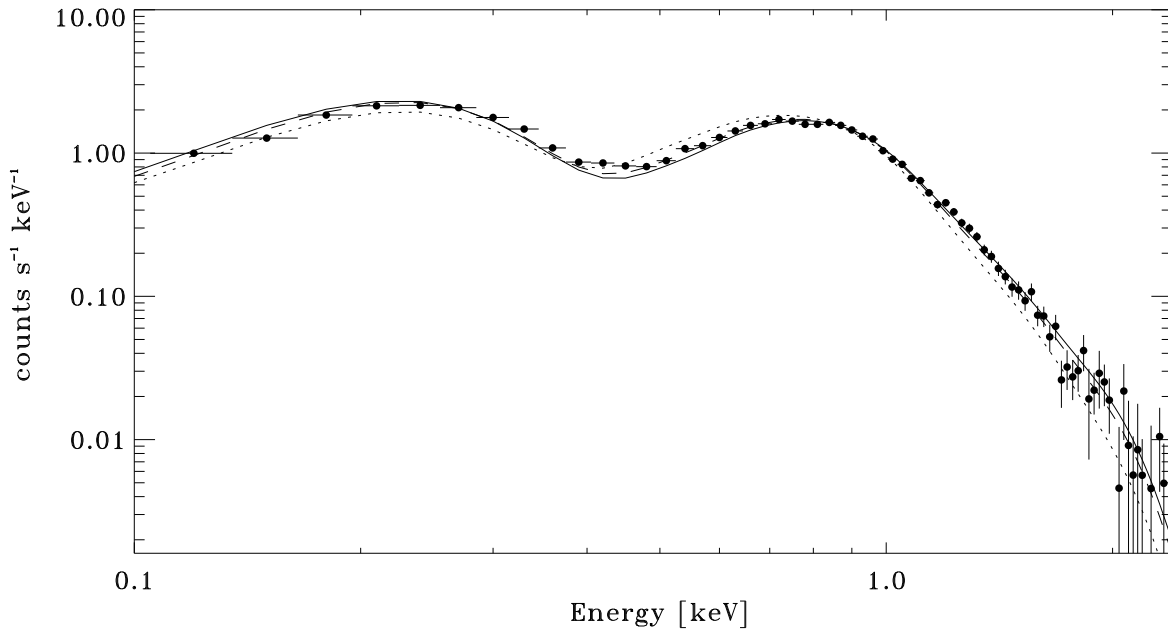
Fig. 12. Spectrum and fits of ζ Ori, cf. Fig. 10.

Table 2. Derived post-shock temperatures and volume filling factors for the O stars from Table 1; both for the present wind model which assumes radiative and adiabatic shock cooling zones, and for the one- and two-component isothermal shock models after Hillier et al. (1993).

| | | cooling zones | isothermal | |
			2-comp.	1-comp.
ζ Pup	$\log T_s =$	6.75	6.64 / 6.20	6.54
	$e_s [10^{-3}] =$	4.3	6.8 / 4.4	11
ι Ori		6.68	6.58 / 6.14	6.43
		35	53 / 31	96
ζ Ori		6.68	6.57 / 6.27	6.46
		5.0	7.9 / 4.3	14

model with resolved cooling zones. – The reason for (a) is that the Raymond-Smith function at energies $0.1 \lesssim E \text{ [keV]} \lesssim 0.5$ and temperatures $6.3 \lesssim \log T \lesssim 6.7$ can be very roughly approximated (cf. Fig. 3) by $\Lambda_\nu(T) \approx A_\nu T^\alpha$, with $\alpha \gtrsim -1/2$. This implies a comparable contribution from both the hotter and colder component to the soft X-ray flux, i.e., the total filling factor is the sum of the individual filling factors. – The main reason for (b) is the density stratification of the cooling zone: for simplicity we consider only radiative shocks, and use $h(\xi) = \xi^{2/7}$ as an approximation to (11). We suppose that the frequency *integrated* emission from a radiative shock and an isothermal shock should be equal. For the cooling function from (7), with exponent $\alpha = -1/2$, Eqs. (1) and (2) give then

$$(e/\sqrt{T})_{\text{iso}} = 7\sqrt{3}\,(2 - \sqrt{3})\,(e/\sqrt{T})_{\text{rad}} \approx 3.2\,(e/\sqrt{T})_{\text{rad}}. \quad (27)$$

Since the temperatures are fixed from the spectral fits, where typically $T_{\text{rad}} \approx 1.7\,T_{\text{iso}}$ results (cf. item 1), we are left with $e_{\text{iso}} \approx 2.5\,e_{\text{rad}}$, in good agreement with the above figure of 2.7.

(3) Fit quality: Our fits with 2 adjustable parameters are better than (or, in the case of ζ Ori, equally as good as) the one-component fits of Hillier et al. (also 2 parameters), and are almost as good as their two-component fits (4 parameters). This is one of the main results of the present paper. – Actually, we find that the two-component Hillier et al. model has too many free parameters, in that the temperature of the hotter component is often left unconstrained by the fit procedure by orders of magnitude. The fits are then to be considered somewhat fortuitous. Furthermore, we note that the one-component fit for ζ Ori is already very good, and only minor achievements can be won from the other two models. ζ Ori seems to be exceptional in this respect since no other star in our full sample can be fitted equally well with a one-temperature model.

As was discussed in the foregoing sections, time-dependent hydrodynamic simulations of hot star winds indicate (i) that reverse shocks are generally stronger than forward shocks; and (ii) that the reverse shocks are abruptly destroyed at relatively small radii, instead of being gradually transformed into adiabatic shocks at large radii. We simulate this shock destruction by applying $r_0 = 8\,R_*$ (cf. Section 2.2) in our fit procedure, since in a first, crude approximation the leftover, adiabatic cooling gas can again be viewed as an SA cooling layer. This gives almost identical results to the ones in Table 2: the derived temperatures and filling factors differ by $\approx 10\%$ only, and the fit quality is about equal. To test the importance of item (i), we assume $\Theta = 10$ for adiabatic shells, instead of $\Theta = 1$ above. Using a large r_0 from stationary wind densities (cf. Eq. 13), the fit quality is again comparable to the one from Figs. 10 to 12 (however, usually not

as good), and the derived temperatures and filling factors differ by $\approx 30\%$. Finally, applying both $r_0 = 8\,R_*$ and $\Theta = 10$ at once results in definitely poorer fits, and the derived parameters differ by $\approx 40\%$ from the ones in Table 2. – However, we do not consider either Θ or r_0 to be adequate fit parameters; instead they should be fixed to plausible values. Valuable information in this respect may – hopefully – be gained from time-dependent hydrodynamic wind simulations.

The question remains as for the influence of the interstellar column density on our results. Varying $\log N_\mathrm{H}$ within the estimated error bounds of Shull & van Steenberg, $\Delta \log N_\mathrm{H} =$ (ζ Pup: ± 0.05; ι Ori: ± 0.15; ζ Ori: ± 0.1), alters the temperatures by $\Delta \log T_\mathrm{s} = (\mp 0.01; \mp 0.08; \mp 0.06)$, and the filling factors by $\Delta e_\mathrm{s} = (\pm 0.2; \pm 10; \pm 1) \times 10^{-3}$ for the model with cooling zones. Recently, Haser (1995) derived a column density to ζ Ori of $\log N_\mathrm{H}\ [\mathrm{cm}^{-2}] = 20.34$, which is slightly off the error interval of Shull & van Steenberg (1985). This low N_H results in a somewhat poorer fit: because the free-free opacity drops $\approx E^{-3}$, the hard part of the spectrum is practically left unaltered – and so should be the fit parameters. On the other hand, the soft X-ray flux is enhanced by lowering the column density, and deviates from the ROSAT data then. Assuming that the true N_H to ζ Ori lies at the lower edge of values allowed by Shull & van Steenberg (1985), our shock temperature for ζ Ori from Table 2 would be 15% too low, and the filling factor 25% too high.

Finally we add some comments about the fit quality near the dip at 0.4 keV. As mentioned above, we ignored the data points in this neighborhood due to calibration uncertainties in the detector response. If, on the other hand, these data points are included, the largest deviations between model and observation are found if helium is fully ionized throughout the wind. The reason is that in the latter case the K-shell opacity is the dominant opacity source at energies around 0.4 keV. Preliminary test calculations indicate that especially a change in carbon abundance can have a large effect on the dip due to its proximity to the C IV K-shell edge at 0.347 keV. But even the nitrogen and oxygen K-shell edges which are located at somewhat higher energies can affect the dip. The reason is that monochromatic photons are spread out over several detector channels. Future work will have to show to what degree this can remove deviations between model and observation at energies near 0.4 keV.

We close this section with a comparison of our method and results with those of Cohen et al. (1996). These authors used both ROSAT and EUVE data to constrain high-temperature emission models for the B giant ϵ CMa (B2 II). They arrived at the strong conclusion that the simplest model (from a hierarchy of increasing complexity) to fit both the X-ray spectrum and the five observed EUV iron emission lines between ≈ 40 and 70 eV simultaneously is one where: (i) the hot gas is distributed through a cold background wind, (ii) the opacity of this cold wind for EUV radiation and soft X-rays is included, and (iii) the emitting plasma has a continuous temperature distribution. Contrary, a two-temperature model is not sufficient. The total number of free parameters of this fit model is five, where $\dot{M}/v_\infty$ is taken as a free parameter which characterizes the wind atten-

uation. Notice that all three items (i) to (iii) are also specific to the model presented here.

Cohen et al. make a power-law Ansatz for the temperature dependence of the differential emission measure, $Q \propto T^a$, where Q is defined as $Q(T) \equiv n_\mathrm{p} n_\mathrm{e} \mathrm{d}V/\mathrm{d}T$, i.e.

$$\epsilon_\nu = \int n_\mathrm{p} n_\mathrm{e}\, \Lambda_\nu(T)\, \mathrm{d}V = \int Q(T)\, \Lambda_\nu(T)\, \mathrm{d}T. \tag{28}$$

Translating this to our approach from Sec. 2 where temperature changes are due to (radial) cooling zones only, $T = T(\xi)$, but where the shock-temperature is *not* a function of radius, we have

$$Q \propto f^2 \frac{\mathrm{d}\xi}{\mathrm{d}g} \propto \frac{1}{g^2 g'}\ , \tag{29}$$

with the functions f and g – where $T \propto g$ – defined in (2), and $g' \equiv \mathrm{d}g/\mathrm{d}\xi$. In the second proportionality of (29) we made use of the approximation that the pressure is almost constant in the cooling zone, $f \propto 1/g$, cf. (8) and (26). For radiative shocks then, from (11), $g \propto \xi^{2/7}$, i.e. $g' \propto g^{-5/2}$, or $a = 1/2$. In contrast, for adiabatic shocks, g is seen from (26) to vary between $g \propto \xi^2$ and $g \propto \xi^{2/3}$, which corresponds to $a = -5/2$ and $a = -3/2$, respectively. Cohen et al. (1996) found from their fits $a = -0.8 \pm 0.35$, which lies within this range of a-values for radiative vs. adiabatic shocks. We can even push this argument further. Our calculated X-ray spectra in the present paper are dominated by inner radiative shocks, with the outer adiabatic shocks serving more or less as a correction term to the soft X-ray flux. On the other hand Cohen et al. analyze a rather thin wind with $\dot{M} \approx 2\ldots 6 \times 10^{-8}\ M_\odot/\mathrm{yr}$, and correspondingly derive filling factors of $\lesssim 0.1$ which are larger than our values in Table 2. (Notice that the global filling factor of Cohen et al. 1996 is identical to our local filling factor since the latter is assumed to be radius independent.) Both the low $\dot{M}$ and the rather large filling factor are hints that cooling by adiabatic expansion may already be competitive to radiative cooling in this B star wind at low heights – which in turn could be a plausible explanation why the value for a of Cohen et al. lies between the above values for radiative vs. adiabatic shocks. However, this is speculation since in principle we believe that some kind of radial temperature stratification is realized in the wind; our claim is therefore only that our fit model is consistent with the findings of Cohen et al. (1996).

4. Summary

We have generalized the isothermal shock emission coefficient of the X-ray transfer model of Hillier et al. (1993) to include the effects of radiative and adiabatic cooling layers behind shock fronts. Under the assumption that all shocks in the wind have the same temperatures and filling factors, our fits to high-quality ROSAT PSPC spectra of three selected O stars are of about the same quality as the two-component fits of Hillier et al., where the latter authors however had to adjust twice as many parameters. Furthermore, the shock temperatures and filling factors

derived from the two-component model are consistent with the temperature and density stratification of cooling zones. This supports the idea that the observed two- (or multi-) component X-ray spectra can be traced back to such stratified cooling zones. However, we cannot exclude an additional contribution from a radius-dependency of shock temperatures and filling factors.

Our model establishes a robust framework within which certain X-ray properties of hot stars – here: temperatures and filling factors – are defined, probably in an averaged sense. Therefore, it should be adequate to *analyze* the sample of ROSAT PSPC observations of 42 O stars. However, the model is meant as a first approximation only to the real structures which emit X-rays in hot star winds. A discussion of such possible flow phenomena, including shell collisions and 'old' hot gas leftover from shock destruction, is given in Feldmeier (1995).

The ROSAT data pose severe constraints on hydrodynamic models which try to *synthesize* the X-ray spectra from the emission of instability-generated shocks. The most serious concern is the rather small amount of hot gas usually predicted from these models, with filling factors being one or two orders of magnitude below those derived from spectral fits; but this could be the result of our present lack of knowledge of the trigger mechanism. The spectrum synthesis from time-dependent hydrodynamic wind models will be the subject of a forthcoming paper.

Appendix A: inner and outer mass flow of the adiabatic shell

Here we derive an approximate expression which relates the properties of an adiabatic SA shell with the jump in the mass loss rate of the star at the time the shell is released.

Using (17), the mass flow $\dot{M} = 4\pi r^2 \rho v$ through a sphere of radius r can be written as

$$S \equiv \eta \sigma V = \frac{\dot{M}}{4\pi v_f \rho_0}, \tag{A1}$$

where S is the dimensionless mass flux. Since S and $\dot{M}$ are constant outside the shell, we have (using $\rho_0 \equiv \rho_{f,pr} r_f^2$)

$$\dot{M}_{\text{source}} = \dot{M}_{\text{in}} = 4\pi \rho_{f,pr} r_f^2 v_\infty \frac{v_f}{v_\infty} S_{\text{in}} = \dot{M}_{\text{out}} \frac{v_f}{v_\infty} S_{\text{in}}, \tag{A2}$$

where $\dot{M}_{\text{source}}$ is the mass flux of the source at $r = 0$, and $\dot{M}_{\text{in}}$ (resp. $\dot{M}_{\text{out}}$) is the mass flow ahead of the reverse (resp. forward) shock. Using (18), we have

$$\frac{\dot{M}_{\text{in}}}{\dot{M}_{\text{out}}} = \frac{1}{1 - \kappa_f} S_{\text{in}}. \tag{A3}$$

This ratio is infinite in SA since they used $v_\infty = 0 = \dot{M}_{\text{out}}$. Applying the usual shock jump conditions, and assuming the

analytical SA solution in the neighborhood of the contact discontinuity (their Eq. 11, our Eq. 26) to apply over the whole shell (see Fig. 7 for the accuracy of this approximation), we have finally

$$\frac{\dot{M}_{\text{in}}}{\dot{M}_{\text{out}}} = \frac{1}{1 - \kappa_f} \frac{\eta_r^3}{\Theta} \left(1 + \frac{12}{5} \left[\left(\frac{\eta_c}{\eta_r} \right)^3 - 1 \right] \right). \tag{A4}$$

For sufficiently weak shocks $\kappa_f \approx 0$ and $\eta_r \approx \eta_c \approx 1$, and the last equation reduces to a trivial consequence of the presumed pressure constancy inside the shell,

$$\frac{\dot{M}_{\text{in}}}{\dot{M}_{\text{out}}} \approx \frac{T_{\text{po,for}}}{T_{\text{po,rev}}} = \Theta^{-1}. \tag{A5}$$

Appendix B: shock collisions in the outer wind

A SA shell, which is enclosed by two adiabatic shocks, expands on its propagation through the wind: the front of the outer, forward shock propagates faster than the shell center (i.e., the contact discontinuity), whereas the front of the inner, reverse shock propagates slower than the shell center. Therefore, if similar SA shells follow upon each other, every forward shock should eventually overtake the reverse shock ahead of it. The question arises (cf. §2) whether this leads to an outer, hot corona surrounding the star. In this appendix we show that instead the shock collision causes a sawtooth-like sequence of forward shocks to occur. Its filling factor of hot gas is roughly comparable with that of the inner SA shells. However, the forward shocks decay with radius, even if the inner SA shocks have constant strength (at least long before any mutual interactions). Since both the SA shells and the forward shocks are similarity solutions asymptotically (i.e., for large distances between shells or shocks), this illustrates how a shock collision can change the similarity parameter δ. In the absence of detailed knowledge of the wind dynamics, we took this in §2 as a justification to fix the value of δ from the outset.

We set up the following hydrodynamic test of multiple adiabatic shells. The initial data are for a stationary, spherical symmetric wind of constant velocity, and density $\rho \propto 1/r^2$. In the SA solution, a single shell is created by a sudden jump in density and speed at the source location $r = 0$ at time $t = 0$. To create multiple shells instead, we use the step function

$$F(t) = H\left(t \bmod \tau - \tfrac{1}{2}\tau\right), \tag{B1}$$

where H is the Heaviside function, and τ is the time interval between the release of two shells. We apply as an inner boundary condition

$$\begin{aligned} v(r_{\text{min}}, t) &= v_0[1 - F(t)] + v_s F(t), \\ \rho(r_{\text{min}}, t) &= \rho_0[1 - F(t)] + \rho_s F(t). \end{aligned} \tag{B2}$$

The values for v_0, ρ_0 and v_s, ρ_s are chosen from the analytical approximation (26) to the single-shell SA solution for $\kappa_f = 0.1$, and equal post-shock temperatures, $\Theta = 1$. We chose $v_f = 1$ and $\rho_0 = 1/r_{\text{min}}^2$. The temperature of the start
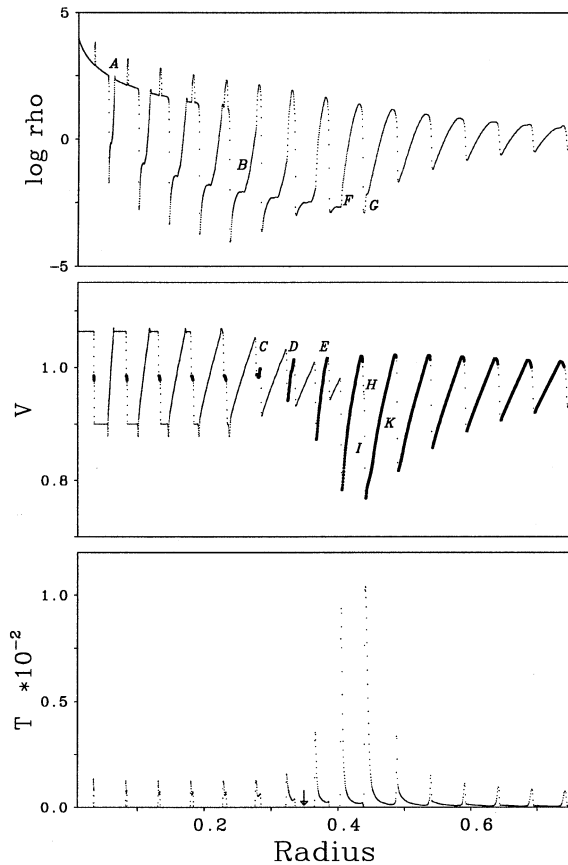
Fig. 13. Hydrodynamic test calculation of multiple SA shells, with a forward/reverse shock merger at $r \approx 0.45$ (normalized units). Dots indicate pre-shock gas, filled circles post-shock gas.

model, and also at the inner boundary over the course of time, is $T = 10^{-8}(1 - \kappa_f)^2/\gamma$ (we use units $k = m_p = 1$ here, so that $T_{po} = \frac{3}{16}\kappa_f^2$), resulting in strong shocks of Mach number $\approx 10^3$. Finally, $\tau = 0.05$ is chosen, which results in a shock collision at $r \approx 0.45$. We use 5,000 logarithmically spaced grid points from $r_{min} = 0.01$ to $r_{max} = 1$. As long as the relative speed of forward and reverse shocks remains constant, the logarithmic grid ensures a shell to be equally well resolved at all radii, since both the grid distance and the shell extension grow $\propto r$. (In Fig. 13, already 1330 grid points lie in between r_{min} and the location of the first reverse shock.) The model is followed up to a time $t = 4$, corresponding to 4 flow times from the inner to the outer grid boundary. However, even at $t = 1$ the flow structure is almost identical to the one in Fig. 13. We used a time-explicit hydrodynamics code which solves the continuity, momentum, and energy equations in integrated form on a staggered grid by applying van Leer (1977) advection. For details we refer to Reile & Gehren (1991) and Feldmeier (1995).

We find from this simulation that the shock collision transforms the inner shell sequence into an outer forward shock sequence, where the latter decays with radius. We now look into this transformation in some more detail.

1. The use of a step function creates two forward facing rarefaction waves (cf. Courant & Friedrichs 1948; Zel'dovich & Raizer 1967) with a linear velocity law between subsequent shells, seen at A or B in Fig. 13. The waves are separated from each other by a region of $v(r, t) = r/t$, $\rho(r, t) = \mathrm{const}/t^3$ (the density plateau at B). A forward shock occurs both at the tail of the inner and at the head of the outer wave. (The shocks appear to be isothermal since their cooling zones are not resolved. We will not refer to these shocks any more in the following, but only to the shell enclosing shocks.) Fluid particles propagate through this whole domain from right to left. Notice that at A the rarefaction waves and the shell shocks are still separated by regions of stationary wind ($v = \mathrm{const}$ and $\rho \propto 1/r^2$), while at B and beyond they are in contact.

2. The velocity law of the rarefaction waves causes a decreasing pre-shock speed at both shocks from about C on. The shocks 'project' this velocity law into the post-shock domain, cf. D and beyond. In this way, the forward shock is accelerated, and the reverse shock is decelerated. At this stage, the shocks move away from the shell center in a symmetric fashion.

3. However, from E on an asymmetry shows up between forward shocks (getting weaker, and less accelerated) and reverse shocks (getting stronger, and more strongly decelerated). The reason is that the forward shock propagates into a strongly increasing density stratification, the reverse shock into a decreasing stratification.

4. From F to G, the reverse shock propagates through the broad density minimum, and sweeps up the gas located there. H and I show the forward and reverse shock just before merging.

5. Beyond K then, only forward shocks exist, which decay with radius. Finally, notice that for the inner shell sequence a gas element can undergo at most one shock transition by entering a shell, while for the outer forward shock sequence every gas element undergoes repeated shock transitions. This is indicated in the velocity diagram of Fig. 13 by marking pre-shock gas with dots, and post-shock gas with filled circles.

This sequence of events depends somewhat on the special boundary conditions (step function) chosen. However, by applying instead a power law decline in source conditions after shell throw-off, the shell sequence is again transformed into a forward shock sequence, so that this result should hold quite generally. Notice that the use of a power law leads to decelerated shells which can no longer be described by the SA similarity variable (16).

References

Berghöfer T.W., Schmitt J.H.M.M., 1994, ApSS 221, 309
Berghöfer T.W., Baade D., Schmitt J.H.M.M., et al., 1996, A&A 306, 899
Carlberg R.G., 1980, ApJ 241, 1131
Chevalier R.A., Imamura J.N., 1982, ApJ 261, 543 (CI)
Cohen D.H., Cooper R.G., MacFarlane J.J., et al., 1996, ApJ 460, 506
Courant R., Friedrichs K.O., 1948, Supersonic flow and shock waves. Interscience Publishers, New York
Cox D.P., Tucker W.H., 1969, ApJ 157, 1157
Daltabuit E., Cox D., 1972, ApJ 173, L13

Drew J.E., Denby M., Hoare M.G., 1994, MNRAS 266, 917

Feldmeier A., 1995, A&A 299, 523

Field G.B., 1965, ApJ 142, 531

Haser S., 1995, PhD thesis, Universität München

Hillier D.J., Kudritzki R.P., Pauldrach A.W., et al., 1993, A&A 276, 117

Krolik J.H., Raymond J.C., 1985, ApJ 298, 660

Kudritzki R.P., Simon K.P., Hamann W.R., 1983, A&A 118, 245

Kudritzki R.P., Palsa R., Feldmeier A., Puls J., Pauldrach A.W.A., 1996, in: Zimmermann H.U., Trümper J., Yorke H. (eds.) Röntgenstrahlung from the universe. MPE Report 263, Garching, p. 9

Lamers H.J.G.L.M., Leitherer C., 1993, ApJ 412, 771

Langer S.H., Chanmugam G., Shaviv G., 1981, ApJ 245, L23

Langer S.H., Chanmugam G., Shaviv G., 1982, ApJ 258, 289

Lucy L.B., 1984, ApJ 284, 351

Lucy L.B., Solomon P.M., 1970, ApJ 159, 879

Moffat A.F.J., Owocki S.P., Fullerton A.W., St-Louis N. (eds.), 1994, Instability and variability of hot star winds. Kluwer, Dordrecht

Owocki S.P., 1992, in: Heber U., Jeffery S. (eds.) The atmospheres of early-type stars. Springer, Heidelberg, p. 393

Owocki S.P., Rybicki G.B., 1984, ApJ 284, 337

Owocki S.P., Rybicki G.B., 1985, ApJ 299, 265

Owocki S.P., Castor J.I., Rybicki G.B., 1988, ApJ 335, 914

Pauldrach A.W.A., Kudritzki R.P., Puls J., Butler K., Hunsinger J., 1994, A&A 283, 525

Puls J., Kudritzki R.P., Herrero A., et al., 1996, A&A 305, 171

Raymond J.C., Smith B.W., 1977, ApJS 35, 419

Raymond J.C., Cox D.P., Smith B.W., 1976, ApJ 204, 290

Reile C., Gehren T., 1991, A&A 242, 142

Shull J.M., van Steenberg M.E., 1985, AJ 294, 599

Simon M., Axford W.I., 1966, Planet. Space Sci. 14, 901 (SA)

Van Leer B., 1977, J. Comp. Phys. 23, 276

Voels S.A., Bohannan B., Abbott D.C., Hummer D.G., 1989, ApJ 340, 1073

Zel'dovich Ya.B., Raizer Yu.P., 1967, Physics of shock waves and high-temperature hydrodynamic phenomena. Academic Press, New York